Electromagnetic Inverse Scattering With Perceptual Generative Adversarial Networks

Rencheng Song, *Member, IEEE*, Youyou Huang, Kuiwen Xu, *Member, IEEE*, Xiuzhu Ye, *Member, IEEE*, Chang Li, *Member, IEEE*, and Xun Chen, *Senior Member, IEEE*

***Abstract*—In this work, we introduce a learning-based method to achieve high-quality reconstructions for inverse scattering problems (ISPs). Particularly, the proposed method decouples the full-wave reconstruction model into two steps, including coarse imaging of dielectric profiles by the back-propagation scheme, and a resolution enhancement of coarse results as an image-to-image translation task solved by a novel perceptual generative adversarial network (PGAN). A perceptual adversarial (PA) loss, which is defined as a perceptual loss for the generator network using hidden layers from the discriminator network, is employed as a structural regularization in PGAN. The PA loss is further combined with the pixel-wise loss, and also possibly the adversarial loss, to enforce a multi-level match between the reconstructed image and its reference one. The adversarial training of the generator and discriminator networks ensures that the structural features of targets are dynamically learned by the generator. Numerical tests on both synthetic and experimental data verify that the proposed method is highly efficient and it achieves superior imaging results compared to other data-driven methods. The validation of the proposed PGAN on ISPs also provides a fast and high-precision way for solving other physics-related imaging problems.**

***Index Terms*—Inverse scattering, generative adversarial networks, perceptual adversarial loss.**

I. Introduction

INVERSE scattering problems (ISPs) detect the geometric and constitutive parameters of unknown scatterers through measured scattered field, which are commonly required in many applications [1]–[3]. The ISPs can be quickly solved by simplified linear models like Born approximation method [4] and back-propagation (BP) method [5] etc. However, these fast methods usually have strong requirements on prior information and they may get failure inversion due to high nonlinearity and ill-posedness of ISPs [6]. Consequently, nonlinear iterative algorithms, which solve complete full-wave models, are more robust and have wider range of applications. There are many typical nonlinear iterative algorithms, such as distorted Born iterative method (DBIM) [7], contrast source inversion (CSI) [8] and subspace-based optimization method (SOM) [9]. These methods can achieve high-quality reconstructions, while the drawback of this kind of methods is that they are usually time-consuming due to high computational complexity.

The ISP algorithms need essentially to build a nonlinear mapping between the scattered field and the unknown constitutive parameters of the scatterers. As known, neural network has been verified to be a powerful tool to build nonlinear mappings. Since the 1990 s, there have been a lot of papers [10]–[12] using artificial neural networks (ANN) to solve ISPs. However, these methods usually highly depend on the prior knowledge of the scatterers [13], and thereby greatly limiting their applications. Recently, inspired by the powerful representation capabilities of deep neural networks (DNN) [14]–[16], the convolutional neural network (CNN), has been successfully applied to solve ISPs, which is denoted as the deep learning based inverse scattering (DL-IS) methods. The DL-IS methods can be generally divided into two categories. One type of DL-IS methods [17], [18] aim to replace the most difficult part of traditional nonlinear iterative algorithms with the trained neural networks. The full inversion algorithm still follows an iterative framework. The other type of existing DL-IS methods consider the ISPs as an image-to-image translation problem [19], [20]. Namely, coarse input images are firstly converted from the scattered field using some non-iterative methods, which are further mapped through various CNNs to get high-resolution reconstructions. We focus on the latter ones in this paper.

Although the results of DL-IS methods are encouraging, this type of post-processing methods are still in its infancy. Researchers have tried various efforts to improve the results of DL-IS methods. A direction of improvement is to adjust the input and output of the network to introduce more useful information or reduce the complexity of the mapping. For example, Zhang *et al.* [21] introduced a hybrid input scheme to enhance the

Manuscript received February 2, 2021; revised May 10, 2021; accepted June 22, 2021. Date of publication June 30, 2021; date of current version July 23, 2021. The associate editor coordinating the review of this manuscript and approving it for publication was Dr. Ilaria Catapano. This work was supported in part by the National Natural Science Foundation of China under Grants 61922075 and 41901350, in part by the Anhui Key Project of Research and Development Plan under Grant 202104d07020005, in part by the Provincial Natural Science Foundation of Anhui under Grant 2008085QF285, and in part by the Fundamental Research Funds for the Central Universities under Grants PA2021KCPY0051 and JZ2021HGTB0078. *(Corresponding author: Xun Chen.)*

Rencheng Song, Youyou Huang, and Chang Li are with the Anhui Province Key Laboratory of Measuring Theory and Precision Instrument, Hefei Anhui 230009, China, and also with the Department of Biomedical Engineering, Hefei University of Technology, Hefei 230009, China (e-mail: dr.rcsong@gmail.com; huangyy@mail.hfut.edu.cn; changli@hfut.edu.cn).

Kuiwen Xu is with the Engineering Research Center of Smart Microsensors and Microsystems, Ministry of Education, Hangzhou Dianzi University, Hangzhou 310018, China (e-mail: kuiwenxu@hdu.edu.cn).

Xiuzhu Ye is with the School of Information and Electronics Engineering, Beijing Institute of Technology, Beijing 100081, China (e-mail: xiuzhuye@outlook.com).

Xun Chen is with the Department of Neurosurgery, The First Affiliated Hospital of USTC, Hefei, Anhui 230001, China, Division of Life Sciences and Medicine, Hefei, Anhui 230027, China, and also with the Department of Electronic Engineering and Information Science, University of Science and Technology of China, Hefei, Anhui 230001, China (e-mail: xunchen@ustc.edu.cn).

Digital Object Identifier 10.1109/TCI.2021.3093793

commonly used BP input feature map. Wei *et al.* [22] took the induced current instead of the dielectric image as the input. Yao *et al.* [23] proposed a two-step DL-IS method to construct the coarse image with the first neural network and they took another neural network for further enhancement of the resolution. The authors also introduce a single convolutional encoder-decoder network to directly map the scattered field to the contrast of scatterers [24].

In addition, adjusting the objective function by adding regularization terms also has an important impact on the imaging quality. The existing DL-IS methods usually train CNNs using a pixel-wise loss to measure the discrepancy of generated image and the target one [20]. This may lead to artifacts in the reconstruction since there is lack of explicit constraints on high-level features of images. Considering this reason, Huang *et al.* [25] introduced the structural similarity (SSIM) loss combining with the pixel-wise mean squared error (MSE) loss to enforce the match of high-level features of the generated image with the reference one. Differently, Ye *et al.* [26] proposed to use the generative adversarial network (GAN) [27] to solve ISPs with inhomogeneous background. The adversarial loss defined in GAN can enforce the generator network to learn high-level features of the target and thereby generate realistic images with guidance from a discriminator network.

Besides the SSIM loss and the adversarial loss, the perceptual loss is another popular way to enforce a direct match of high-level features between the reconstructed image and its ground truth. The high-level features are usually defined as hidden layers of a neural network. Perceptual loss has been proven to have an apparent effect on improving the quality of generated images in other fields. For example, Ledig *et al.* [28] combined the adversarial loss and the perceptual loss [29] to generate realistic pictures in the image super-resolution task. Yang *et al.* [30] took the GAN with a perceptual loss to solve the low-dose CT image denoising problem. In these papers, the perceptual loss is usually defined with hidden layers of some pre-trained networks such as VGG-Net. In contrast, Wang *et al.* [31] introduced a perceptual adversarial network (PAN) to define perceptual losses with hidden layers from the discriminative network instead of the ones from pre-trained networks. This effectively improves the ability of the hidden layers to represent features of target images compared to the ones from the pre-trained networks.

Inspired by the success of existing works, in this paper, we propose a new DL-IS method to reconstruct scatterer profiles. The proposed method is composed of two steps, including coarse reconstructions of profiles from scattered field by non-iterative methods and a further refinement through a novel perceptual generative adversarial network (termed as PGAN). The PGAN is composed of a U-net-like [32], [33] generator network and a PatchGAN-like [34] discriminator network. The coarse images obtained by the back-propagation are taken as inputs for the generator to reconstruct realistic profiles. The discriminator learns to differentiate the reconstructed image and the reference profile. The perceptual adversarial loss, which is defined using the hidden layers from the discriminator, can guide the reconstruction of the generator through explicit feature matching. It is combined with the pixel-wise loss, and also possibly the adversarial loss, to train the PGAN networks in an adversarial way. The loss functions are expected to enforce the generator to learn multi-level features of the target image. The proposed method is tested with both synthetic and experimental data. The results verify the superior performance of PGAN over other methods.

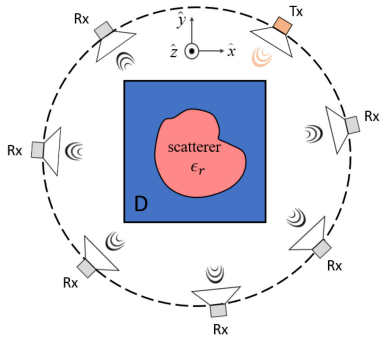

Fig. 1. The configuration of 2-D ISPs under TM illuminations.

It should be noted that the proposed PGAN is specially designed for ISPs, and it is different from the PAN introduced in [31] in both network structures and loss functions. In summary, the benefits of the proposed method are listed as follows. First, we introduce a perceptual generative adversarial network to solve ISPs. The perceptual adversarial loss together with the pixel-wise loss are taken to explicitly enforce a multi-level match between the reconstructed image and the target one, and thereby significantly improving the reconstruction quality. Second, we compare the proposed method with several typical GAN-based methods on different types of measurements. The comparison results verify the advantages of the proposed method in terms of both accuracy and generalization capability. Third, the PGAN is potentially useful for solving other physics-based image translation problems like the CT denoising [30] and diffraction tomography [35] etc, which require the match of both pixel values and high-level features.

This structure of this paper is constructed as follows. We firstly describe the formulation of the ISPs and then introduce the proposed PGAN algorithm in Section II. The method is then compared with other ones for both synthetic and experimental data in Section III. Finally, we conclude our work in Sections IV.

II. Method

A. Formulation of the Problem

The configuration of the current study is depicted in Fig. 1. For convenience of demonstration, we consider a two-dimensional (2-D) transverse magnetic (TM) [36] ISPs. The unknown scatterer is supposed to be located in a square domain of interest (DOI) D. The relative permittivity of the lossless dielectric scatterer is denoted as ϵ_r and the background is free space with permittivity as ϵ_0. There are N_i transmitter antennas and N_r receiver antennas located evenly surrounding the DOI.

As shown in Fig. 1, one transmitter antenna Tx emits electromagnetic waves, which are scattered with the unknown scatterers in DOI D, and the related scattered fields are measured by

the surrounding receiver antennas Rx. The transmitting antenna illuminates the DOI D in turn from different directions. The receiving antennas will also record the measured scattered field sequentially. The purpose of ISP is to retrieve the unknown relative permittivity ϵ_r of the scatterers with all the measured scattered field. The mathematical formulations of the forward scattering are introduced as below. For clarity, we first declare the notations of symbols. The vectors and matrices will both be represented in bold. In particular, if necessary, we will further use a single bar and double bars to distinguish vectors and matrices, respectively.

The domain D is discretized into $N = M \times M$ square subunits and we take the method of moments (MOM) [18] to calculate the scattered field. The governing Lippmann-Schwinger equation is discretized as

$$\bar{\mathbf{E}}^{tot} = \bar{\mathbf{E}}^{inc} + \bar{\bar{\mathbf{G}}}_D \cdot \bar{\bar{\boldsymbol{\xi}}} \cdot \bar{\mathbf{E}}^{tot}, \tag{1}$$

where the $\bar{\mathbf{E}}^{tot}$ is the total electrical field in domain D. The $\bar{\mathbf{E}}^{inc}$ is the incident electrical field, $\bar{\bar{\mathbf{G}}}_D$ is the 2-D free space Green's function in D, and $\bar{\bar{\boldsymbol{\xi}}}$ is a diagonal matrix of contrast function.

Eq. (1) can be reformulated as

$$\bar{\mathbf{J}} = \bar{\bar{\boldsymbol{\xi}}} \cdot (\bar{\mathbf{E}}^{\mathrm{inc}} + \bar{\bar{\mathbf{G}}}_D \cdot \bar{\mathbf{J}}), \tag{2}$$

considering the relation $\bar{\mathbf{J}} = \bar{\bar{\boldsymbol{\xi}}} \cdot \bar{\mathbf{E}}^{\mathrm{tot}}$ between the induced current $\bar{\mathbf{J}}$ with the total field $\bar{\mathbf{E}}^{\mathrm{tot}}$.

The scattered field at the locations of receivers outside D can be represented as

$$\bar{\mathbf{E}}^{\mathrm{sca}} = \bar{\bar{\mathbf{G}}}_S \cdot \bar{\mathbf{J}}, \tag{3}$$

where $\bar{\mathbf{E}}^{\mathrm{sca}}$ is the scattered field on the receivers with dimension $N_r \times 1$, and $\bar{\bar{\mathbf{G}}}_S$ is the Green's function with dimension $N_r \times N$ to map contrast source $\bar{\mathbf{J}}$ to scattered field $\bar{\mathbf{E}}^{\mathrm{sca}}$.

B. The PGAN Algorithm

1) Network Structures: The existing DL-IS methods in an image-to-image translation framework usually choose a fast non-iterative algorithm like BP to build the coarse image $\mathbf{x}$. The use of fast BP method can save a lot of computational time compared to the traditional nonlinear inversion methods, which guarantees the overall computational efficiency of DL-IS methods. Then a CNN $G_{\boldsymbol{\theta}}$ such as the well-known U-net is taken to build the nonlinear mapping between the rough input image $\mathbf{x}$ and the reference image $\mathbf{y}$, where $\boldsymbol{\theta}$ denotes the unknown parameters of the network G. A pixel-wise loss is usually taken to optimize the parameters of the CNN. For example, the one based on $L1$ norm can be defined as

$$L_1(\boldsymbol{\theta}) = \|G_{\boldsymbol{\theta}}(\mathbf{x}) - \mathbf{y}\|_1. \tag{4}$$

It is noted that the batch size is omitted for brevity. Similarly, the other loss functions defined in this paper also follow this usage. The readers can also refer to some latest review papers [20], [37] for more details about the existing DL-IS methods.

This type of two-step DL-IS methods avoid directly dealing with measured scattered field data, where the network must spend remarkable cost to train and learn underlying wave physics. The scattered field is converted into coarse image by BP and the ISP is solved in the image domain as an image-to-image translation problem. This effectively reduces the difficulty of building the neural network mapping to reconstruct scatterer profiles. Therefore, the proposed PGAN algorithm introduced next will also take the two-step framework for solving ISPs.

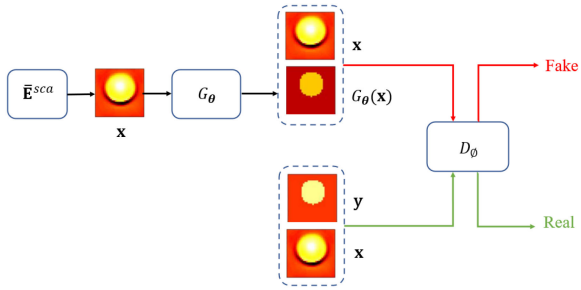

Fig. 2. The flowchart of the full inversion algorithm.

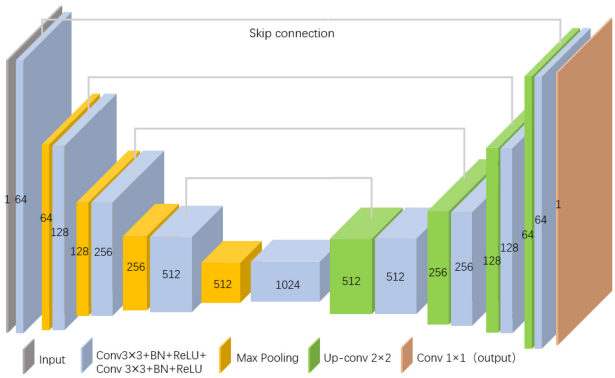

Fig. 3. The structure of the generator for PGAN.

The proposed PGAN algorithm follows a flowchart as Fig. 2 under the GAN framework for solving an image-to-image translation. First, a coarse image $\mathbf{x}$ is constructed from the measured scattered field through the BP method. The coarse image $\mathbf{x}$ is then mapped through the generator $G_{\boldsymbol{\theta}}$ to generate image as $G_{\boldsymbol{\theta}}(\mathbf{x})$ which approximates the reference permittivity image $\mathbf{y}$. The discriminator $D_{\boldsymbol{\phi}}(\mathbf{x}, \mathbf{z})$ is taken to guide the distribution of generations to be consistent with the reference ones, where $\boldsymbol{\phi}$ are the unknown parameters of network D, and $\mathbf{z}$ indicates either the generation $G_{\boldsymbol{\theta}}(\mathbf{x})$ or the reference $\mathbf{y}$. Here the input $\mathbf{x}$ is taken as a condition for the discriminator in order to pair the input and output of the generation. The output of the discriminator is a discrimination matrix like the one used in PatchGAN [34]. The networks $G_{\boldsymbol{\theta}}$ and $D_{\boldsymbol{\phi}}$ are trained alternatively in an adversarial way.

In this paper, the generator is selected as the U-net [33] shown in Fig. 3. The discriminator is illustrated as Fig. 4.

2) Loss Functions: In PGAN method, the loss function for optimizing generator $G_{\boldsymbol{\theta}}$ is defined as

$$L_G(\boldsymbol{\theta}|\boldsymbol{\phi}) = L_1(\boldsymbol{\theta}) + \gamma L_{PA}(\boldsymbol{\theta}|\boldsymbol{\phi}), \tag{5}$$

where $L_1(\boldsymbol{\theta})$ is the pixel-wise loss in (4), γ is the weight to balance the different terms, and $L_{PA}(\boldsymbol{\theta}|\boldsymbol{\phi})$ denotes the perceptual adversarial loss defined for $G_{\boldsymbol{\theta}}$ using $D_{\boldsymbol{\phi}}$ with fixed $\boldsymbol{\phi}$.

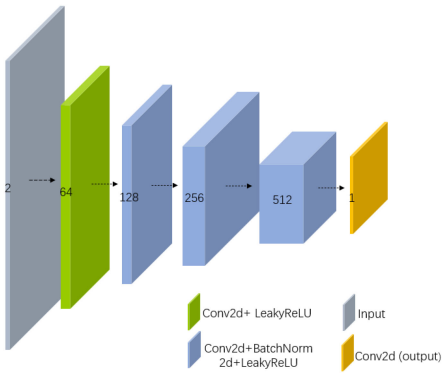

Fig. 4. The structure of the discriminator for PGAN.

The $L_{PA}(\boldsymbol{\theta}|\boldsymbol{\phi})$ in Eq. (5) is defined as

$$L_{PA}(\boldsymbol{\theta}|\boldsymbol{\phi}) = \sum_{j=1}^{M_d} \lambda_j \|\mathbf{d}_{j,\boldsymbol{\phi}}(\mathbf{x}, G_{\boldsymbol{\theta}}(\mathbf{x})) - \mathbf{d}_{j,\boldsymbol{\phi}}(\mathbf{x}, \mathbf{y})\|_1, \quad (6)$$

where M_d is the number of hidden layers used from $D_{\boldsymbol{\phi}}$, $\mathbf{d}_{j,\boldsymbol{\phi}}$ represents the jth hidden layer of the discriminator network $D_{\boldsymbol{\phi}}$, and λ_j is the weight of each perceptual loss to balance the L_1 and perceptual adversarial losses.

In order to investigate the effect of the perceptual adversarial loss with respective to the commonly adversarial loss, we also optimize the generator network with losses in (7),

$$L_G(\boldsymbol{\theta}|\boldsymbol{\phi}) = L_1(\boldsymbol{\theta}) + \beta L_A(\boldsymbol{\theta}|\boldsymbol{\phi}) + \gamma L_{PA}(\boldsymbol{\theta}|\boldsymbol{\phi}), \quad (7)$$

where $L_A(\boldsymbol{\theta}|\boldsymbol{\phi}) = \|D_{\boldsymbol{\phi}}(\mathbf{x}, G_{\boldsymbol{\theta}}(\mathbf{x})) - D_{\boldsymbol{\phi}}(\mathbf{x}, \mathbf{y})\|_1$ is the adversarial loss, and β is the weight. For easy distinction, we denote the method in (7) as PGAN-1, while the one in (5) is as PGAN-2.

As can be observed from the definitions, the L_{PA} loss can guide the reconstructions of the generator network through explicit feature matching, while the L_A loss only regularizes the learning space to enforce patches of the reconstructed image to be overall realistic or not. The two losses are partially redundant with each other to restrict the optimization space. However, from a feature point of view, the use of L_A loss in PGAN-1 further restricts the reconstructed targets from the highest-level of features compared to PGAN-2. The PGAN-1 is expected to address challenging ISP reconstructions with higher nonlinearity. However, the cost is that the training of the model becomes more difficult. In the experiments, we will fully evaluate the performance of PGAN-1 and PGAN-2 for ISP reconstructions to further understand their effects.

The loss function of discriminator $D_{\boldsymbol{\phi}}$ is

$$L_D(\boldsymbol{\phi}|\boldsymbol{\theta}) = \frac{1}{2}\left(\|D_{\boldsymbol{\phi}}(\mathbf{x}, \mathbf{y}) - 1\|_2^2 + \|D_{\boldsymbol{\phi}}(\mathbf{x}, G_{\boldsymbol{\theta}}(\mathbf{x}))\|_2^2\right) + [m - L_{PA}(\boldsymbol{\phi}|\boldsymbol{\theta})]^+, \quad (8)$$

where $\|\cdot\|_2$ indicates the L2 norm, $L_{PA}(\boldsymbol{\phi}|\boldsymbol{\theta})$ is the same as $L_{PA}(\boldsymbol{\theta}|\boldsymbol{\phi})$, except that the fixed parameters are $\boldsymbol{\theta}$, m is a hyperparameter to be assigned, and $[\cdot]^+ = \max(0, \cdot)$. From (8), the third term of L_D will have zero gradient if $L_{PA}(\boldsymbol{\phi}|\boldsymbol{\theta}) \geq m$. If $L_{PA}(\boldsymbol{\phi}|\boldsymbol{\theta}) < m$, the third term of L_D will have the value of $m - L_{PA}(\boldsymbol{\phi}|\boldsymbol{\theta})$. Hence, the value of m is equivalent to setting an upper limit for $L_{PA}(\boldsymbol{\phi}|\boldsymbol{\theta})$.

Algorithm 1: Update algorithm of $G_{\boldsymbol{\theta}}$ and $D_{\boldsymbol{\phi}}$.

1: Initialize the parameters $\boldsymbol{\theta}$ and $\boldsymbol{\phi}$ for $G_{\boldsymbol{\theta}}$ and $D_{\boldsymbol{\phi}}$;
2: Update $D_{\boldsymbol{\phi}}$ through minimizing (8) with fixed $\boldsymbol{\theta}$ in $G_{\boldsymbol{\theta}}$: $\boldsymbol{\phi} \leftarrow \boldsymbol{\phi} - \eta \nabla_{\boldsymbol{\phi}} L_D$;
3: Update $G_{\boldsymbol{\theta}}$ through minimizing (5) or (7) with fixed $\boldsymbol{\phi}$ in $D_{\boldsymbol{\phi}}$: $\boldsymbol{\theta} \leftarrow \boldsymbol{\theta} - \eta \nabla_{\boldsymbol{\theta}} L_G$;
4: Repeat steps 2 and 3 until a stop criterion reached.

3) Update of Parameters: In PGAN, the $G_{\boldsymbol{\theta}}$ and $D_{\boldsymbol{\phi}}$ are optimized alternatively. Namely, the parameters of one network are updated under the condition that the parameters of the other network are fixed. So finally, the updating algorithm of $G_{\boldsymbol{\theta}}$ and $D_{\boldsymbol{\phi}}$ are summarized in Algorithm 1.

C. Computational Complexity

For brevity, we only estimate the computational complexity of PGAN in the testing case, where the BP and the generator network will be run only once to obtain the reconstruction. The computational complexity of the proposed method includes two parts, the complexity of using BP method to obtain a coarse input image from scattered field is labeled as O_1, and the workload of using generator network to further enhance the resolution of input is labeled as O_2.

As mention above, the domain D is discretized into $N = M \times M$ square subunits. The computational complexity for BP method is mainly dominated by computing $\bar{\bar{\mathbf{G}}}_D \cdot \bar{\mathbf{J}}$ in Eq. (2). If fast Fourier transform (FFT) is applied in the matrix-vector multiplication, the computational cost of BP is $O_1(N_i M^2 \log M^2)$ [32], where N_i is the number of incidences.

The computational cost of networks is composed of basic operations like convolutions, activation function, and pooling etc. Particularly, the complexity is dominated by the convolutions among above operations. For a convolutional operation, suppose the number of the input feature maps and output feature maps are Q_i and Q_o, respectively. The computational complexity in the convolution layer of the generator network is in the order of $O_2(M_f^2 K_f^2 Q_i Q_o)$ [32], [38], where $M_f \times M_f$ is the size of the feature map and $K_f \times K_f$ ($K_f = 3$ in this paper) is the convolution kernel size. It is also noted that, all the learning-based methods in Table II take similar computational cost because we use the same network structure.

III. Numerical and Experimental Results

In this section, we choose five examples including both synthetic and experimental data to verify the effectiveness of the proposed algorithm. The Modified National Institute of Standards and Technology (MNIST) [39] data set is taken to train the model for all examples. In the testing phase, we test the trained model for both within-database and cross-database cases.

The proposed methods are compared with some other methods, including the BP, the U-net, the pix2pix [34] and the

original PAN methods [31]. The loss functions of generators in different methods are listed in Table II as a reference. In order to quantitatively evaluate the reconstruction accuracy of all methods, the structure similarity measure (SSIM) in Eq. (9) and the root-mean-square error (RMSE) in Eq. (10) are taken as the quality metrics. Namely,

$$\mathrm{SSIM}(\tilde{\mathbf{y}},\mathbf{y}) = \frac{(2\mu_{\tilde{\mathbf{y}}}\mu_{\mathbf{y}} + C_1)\,(2\sigma_{\tilde{\mathbf{y}}\mathbf{y}} + C_2)}{\left(\mu_{\tilde{\mathbf{y}}}^2 + \mu_{\mathbf{y}}^2 + C_1\right)\left(\sigma_{\tilde{\mathbf{y}}}^2 + \sigma_{\mathbf{y}}^2 + C_2\right)}, \quad (9)$$

where $\tilde{\mathbf{y}}$ and $\mathbf{y}$ are the reconstructed and true relative permittivity profiles, respectively, $\mu_{\mathbf{y}}$ denotes the mean of $\mathbf{y}$, $\sigma_{\mathbf{y}}^2$ is the variance of $\mathbf{y}$, and $\sigma_{\tilde{\mathbf{y}}\mathbf{y}}$ indicates the covariance of $\tilde{\mathbf{y}}$ and $\mathbf{y}$. The C_1 and C_2 are small constants to avoid zero in the denominator, where $C_1 = (K_1 L)^2$ and $C_2 = (K_2 L)^2$ with $K_1 = 0.01$ and $K_2 = 0.03$ as two hyperparameters, and L as the dynamic range of pixel values of the target image $\mathbf{y}$. And

$$\mathrm{RMSE} = \sqrt{\frac{1}{N}\sum_{m=1}^{M}\sum_{n=1}^{M}\left|\frac{\epsilon_{r;m,n}^{r} - \epsilon_{r;m,n}^{t}}{\epsilon_{r;m,n}^{t}}\right|^2}, \quad (10)$$

where $\epsilon_{r;m,n}^{r}$ and $\epsilon_{r;m,n}^{t}$ are the reconstructed and true relative permittivity of the unknown scatterers, respectively, and $N = M \times M$ is the total number of small subunits over the DOI.

A. Configuration of the Scattering System

We test the trained model with five examples. In the first four synthetic examples, the DOI is chosen as a square domain with the size of 2.0 m $\times$ 2.0 m. The frequency is set as 400 MHz, and there are 16 linearly polarized transmitters and 32 line receivers located evenly over the circle at radius of R = 3.0 m. The last experimental example is based on experimental data provided by Institute Fresnel (Marseille, France) [40]. For each incidence, we calculate the scattered field using the MOM method, where DOI is discretized into 100×100 grids. To avoid the inverse crime, the grids used for reconstruction are changed to 64×64.

B. Training Details

The MNIST [39] data set is used as the training data for all examples. We randomly select 5000 images from MNIST as the training set and another 2500 images as the validation set. A random circle with radius from 0.1 m to 0.5 m is also incorporated into each digit to improve the model generalization capability [22]. Meanwhile, each digit is randomly rotated with an angle between -170° and 170° to account for the spatial diversity of scatterers. The scatterers in the training stage are assumed to be lossless dielectrics with relative permittivity ε_r randomly distributed between 1.5 and 2.5, and the background is free space for all examples.

The model is trained using the Adam optimization method with the exponential decay rates set as $\beta_1 = 0.9$ and $\beta_2 = 0.999$, respectively. Some other hyperparameters used for training are listed as follows. The batch size is taken as 1 and the model is trained for 40 epochs. The learning rate is initially set to 0.0002 for the first 20 epochs and it sequentially decreases to zero from the 21st epoch to the last epoch.

The hyperparameters are set as follows. The number of hidden layers M_d is set to 1 to define the L_{PA} loss from D_{ϕ}. This is because the scatterer images in this study are relatively simple compared to natural images. Specifically, the second layer of D_{ϕ} is selected in the experiments as shown in Fig. 4. Meanwhile, the weight parameter λ_j in L_{PA} is set to 4.0 and the hyper-parameter m in L_D is set as 0.2. The β and γ are set to 0.01 and 1.0, respectively, in all methods as listed in Table II.

The code is prepared with PyTorch 1.3 and it is trained and tested on a server with 3.40 GHz Intel(R) Core(TM) i7-6800 K CPU and GeForce GTX 1080Ti GPU. In the training stage, it takes about 3.45 hours to train the proposed networks.

C. Within-Database Test: Synthetic Data

In the first example, we test the trained model with another 1500 images randomly selected in MNIST data set. In addition, 10% Gaussian white noise is added to the scattered field in the test set.

The reconstruction results of Test#1 to Test#4 are shown in Fig. 5, respectively. Meanwhile, the SSIM and RMSE of the compared methods are presented in Table I. From Fig. 5 and Table I, we can see that all data-driven methods have obtained good results, while the PGAN-1 and PGAN-2 methods have achieved better imaging quality in terms of both SSIM and RMSE. In detail, the reconstructed results of the PAN are worse than the other learning-based methods. It indicates that the use of the pixel-wise loss is necessary for physics-related reconstruction task. The comparison results of PGAN-1 and pix2pix methods, and also the comparison between the PGAN-2 and the U-net methods, indicate that the addition of L_{PA} loss enhances the quality of reconstruction for ISPs. For this testing example, the performance of PGAN-2 is slightly better than that of PGAN-1, which indicates the simultaneous use of adversarial loss is not necessary for simple ISPs.

It only takes about 0.86 seconds to achieve a single reconstruction during the testing stage. In detail, the BP takes about 0.14 seconds, while the networks takes about 0.72 seconds. In comparison, the conventional subspace optimization method (SOM) running with 50 iterations takes 39.37 seconds to reconstruct a single case. Regarding memory requirements, the GPU memory usage is about 1.33 G during training, and meanwhile, the computer memory usage is 2.66 G.

D. Cross-Database Test: Synthetic Data

In order to verify the model generalization capability of the proposed methods, we also test the trained model with more challenging examples in a cross-database way. In the following three examples, we use exactly the same model trained in the first example to reconstruct the scatterer. All the other settings also keep the same. The results are shown as below.

1) Complex Profiles: In the second example, we test the trained model on scatterers with complex profiles as shown in Fig. 6, where double rings, double circles, letter P and "Austria" profiles [41] are reconstructed in Test#5-Test#8, respectively. The permittivity of all scatterers in Fig. 6 is 2.0. The error metrics of reconstructions are summarized in Table III. We can see that

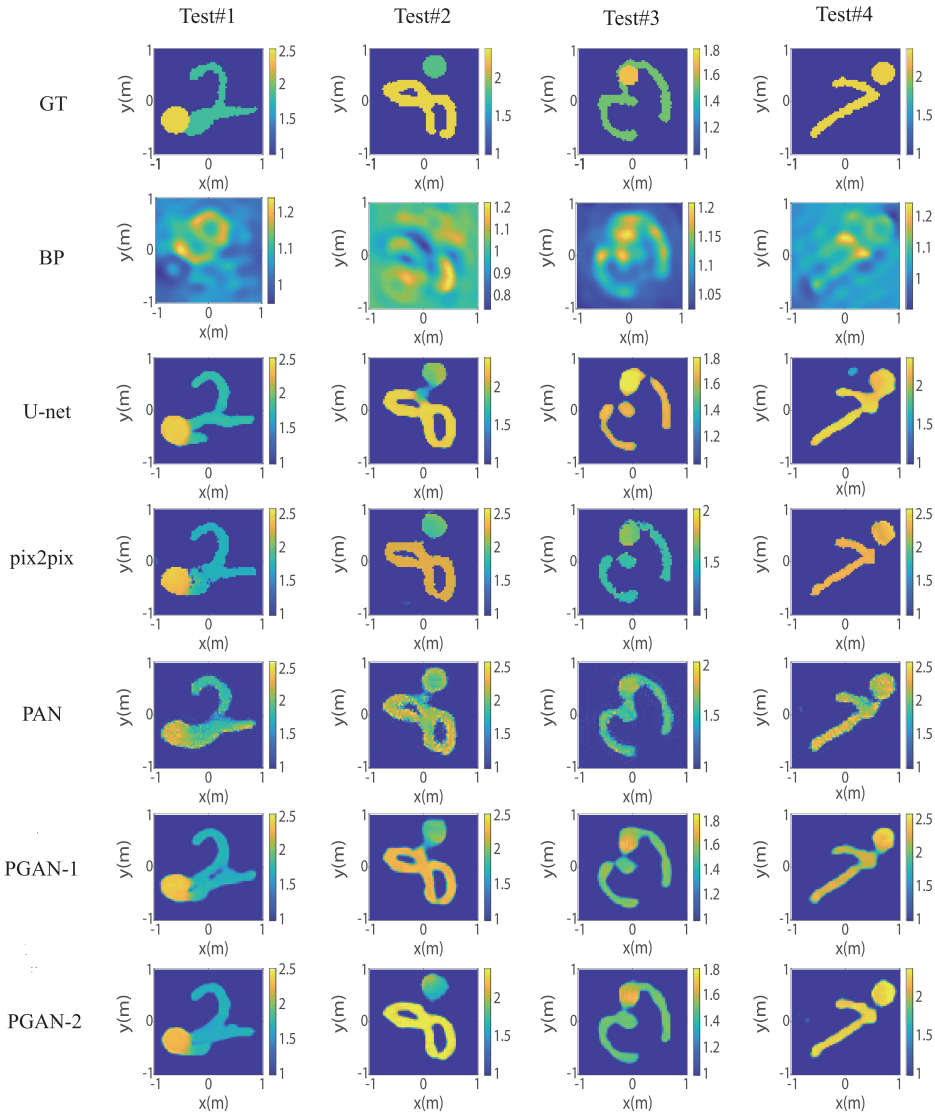

Fig. 5. Reconstruction results of Test#1 to Test#4 from the MNIST data set with 10% Gaussian noise.

TABLE I
ERROR METRICS OF RECONSTRUCTION RESULTS FOR 1500 TESTING SAMPLES FROM MNIST DATA SET BY U-NET, PIX2PIX, PAN, PGAN-1 AND PGAN-2 IN FIG. 5

Method	Test#1		Test#2		Test#3		Test#4		1500 MNIST	
	SSIM	RMSE	SSIM	RMSE	SSIM	RMSE	SSIM	RMSE	SSIM	RMSE
U-net	0.82	0.17	0.85	0.19	0.84	0.09	0.84	0.20	0.87	0.14
pix2pix	0.83	0.15	0.79	0.22	0.85	0.09	0.85	0.20	0.85	0.14
PAN	0.81	0.16	0.81	0.22	0.82	0.10	0.83	0.20	0.82	0.15
PGAN-1	0.81	0.16	**0.86**	0.17	**0.88**	0.08	**0.89**	0.15	0.87	**0.12**
PGAN-2	**0.85**	**0.13**	**0.86**	**0.16**	**0.88**	**0.07**	**0.89**	**0.14**	**0.88**	**0.12**

TABLE II
THE LOSS FUNCTIONS OF GENERATOR G_θ IN DIFFERENT METHODS

Method	U-net	pix2pix	PAN	PGAN-1	PGAN-2
G Loss	L_1	$L_1+\beta L_A$	$\beta L_A+\gamma L_{PA}$	$L_1+\beta L_A+\gamma L_{PA}$	$L_1+\gamma L_{PA}$

the PGAN-1 and PGAN-2 have achieved similar performance in all these cases and both of the two methods outperform the comparison ones. For simple profiles (Test#6), the PGAN-2 achieves the best imaging results, while PGAN-1 method has better reconstructions for relatively complex profiles (Test#5 and Test#8). In general, the PGAN-1 and PGAN-2 methods have achieved better imaging quality compared with other methods. It indicates that the perceptual adversarial loss can also effectively enhance the reconstruction quality of complex profiles.

2) High Noise Interference: In the third example, we investigate the model generalization capability considering high-level noise interferences on the measurements. We conduct the test using the "Austria" profile with a relative permittivity of ε_r

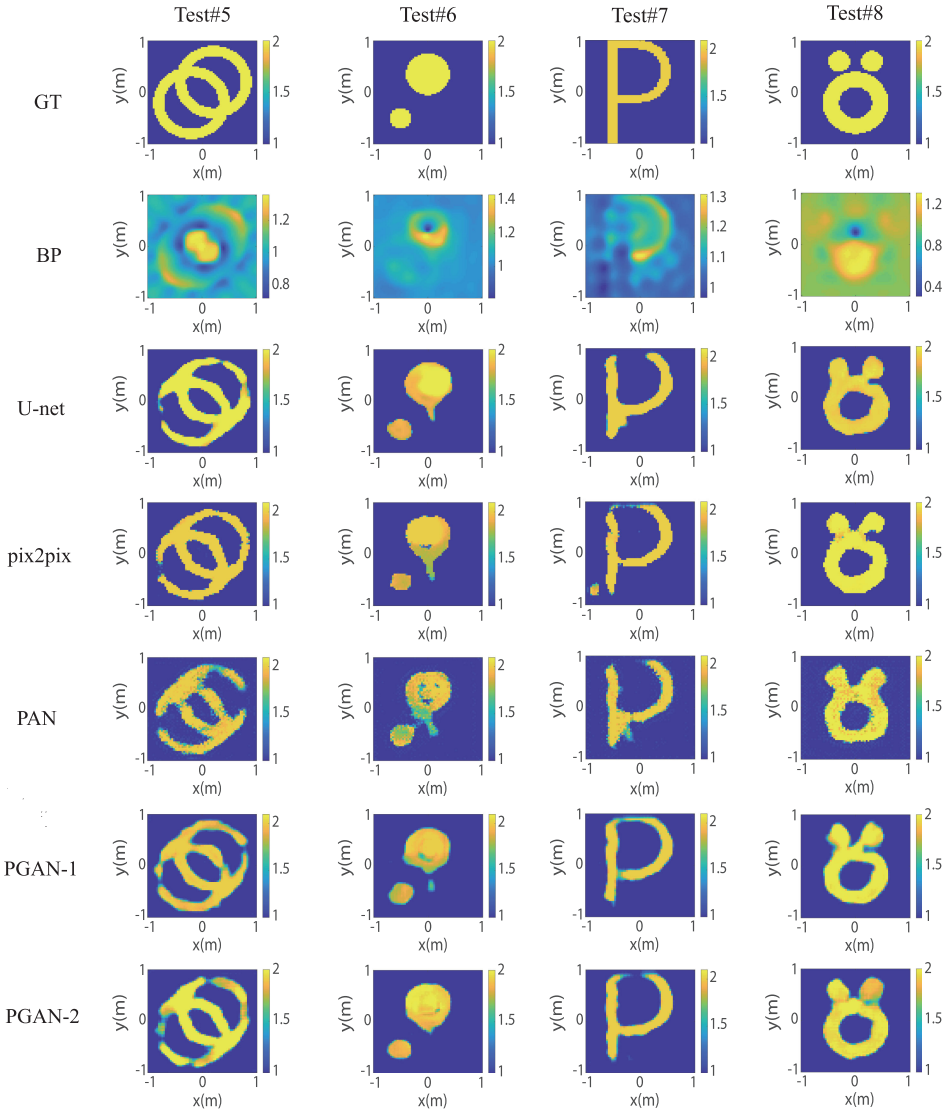

Fig. 6. Reconstruction results of complex profiles with the relative permittivity of 2.0 and 10% noise levels.

TABLE III
ERROR METRICS OF RECONSTRUCTION RESULTS IN FIG. 6 FOR TEST#5-TEST#8

Method	Test#5		Test#6		Test#7		Test#8	
	SSIM	RMSE	SSIM	RMSE	SSIM	RMSE	SSIM	RMSE
U-net	0.60	0.23	0.84	0.15	0.78	0.21	0.72	0.19
pix2pix	0.61	0.22	0.85	0.14	0.77	0.18	0.73	0.19
PAN	0.60	0.22	0.79	0.16	0.75	0.21	0.68	0.20
PGAN-1	**0.67**	**0.20**	0.85	0.13	**0.81**	**0.17**	**0.77**	**0.16**
PGAN-2	0.65	0.22	**0.88**	**0.12**	**0.81**	**0.17**	0.76	0.17

as 1.5. Meanwhile, 10%, 20%, 25% and 30% white Gaussian noises are added respectively to the scattered field to test the robustness of the model. The reconstruction results are shown in Fig. 7 and the corresponding error metrics are summarized in Table IV. It can be seen that the PGAN-1 and PGAN-2 outperform the other comparison methods under different noise levels. Specially, the performance of PGAN-2 is even better than that of PGAN-1 in this example ($\epsilon_r = 1.5$), which is different from the case in Test#8 ($\epsilon_r = 2.0$). In short, this example proves that the proposed methods maintain a good generalization capability of the trained model under high noise interferences.

3) Large Permittivity Range: In the fourth example, we test the proposed methods in a large permittivity range. The relative permittivity of a star profile for Test#13 to Test#16 in Fig. 8 is 1.5, 2.0, 2.5 and 3.0, respectively. The corresponding error metrics are summarized in Table V. We can see that the imaging results of the proposed methods are similar as the U-net for Test#13 and Test#14 with small permittivities. And the PGAN-1 and PGAN-2 outperform the comparison ones in Test#15 and Test#16, where

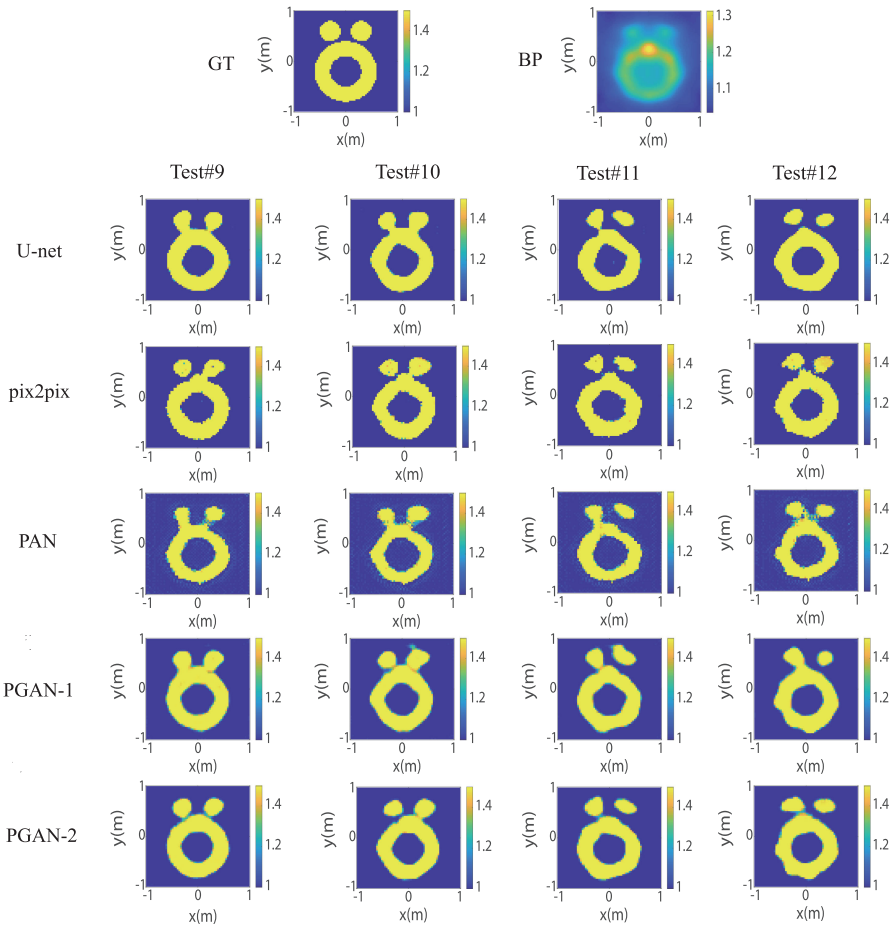

Fig. 7. Reconstruction results of "Austria" profiles under different noise levels. Test#9 to Test#12 are obtained with 10%, 20%, 25% and 30% white Gaussian noise, respectively. The first line shows the ground truth images (left) and the reconstructed result (right) for BP method with 10% noise.

TABLE IV
ERROR METRICS OF RECONSTRUCTION RESULTS IN FIG. 7 FOR "AUSTRIA" PROFILES UNDER DIFFERENT NOISE LEVELS

Method	Test#9		Test#10		Test#11		Test#12	
	SSIM	RMSE	SSIM	RMSE	SSIM	RMSE	SSIM	RMSE
U-net	0.86	0.07	0.81	0.08	0.76	0.10	0.75	0.10
pix2pix	0.82	0.08	0.80	0.09	0.75	0.10	0.75	0.10
PAN	0.74	0.09	0.73	0.09	0.74	0.09	0.69	0.10
PGAN-1	0.86	0.08	0.83	0.08	0.80	0.09	0.77	0.10
PGAN-2	**0.89**	**0.06**	**0.85**	**0.07**	**0.82**	**0.08**	**0.79**	**0.09**

TABLE V
ERROR METRICS OF RECONSTRUCTION RESULTS IN FIG. 8 FOR TEST#13-TEST#16

Method	Test#13		Test#14		Test#15		Test#16	
	SSIM	RMSE	SSIM	RMSE	SSIM	RMSE	SSIM	RMSE
U-net	**0.93**	**0.05**	0.92	0.10	0.80	0.30	0.81	0.33
pix2pix	0.91	0.06	0.91	0.10	0.81	0.28	0.81	0.30
PAN	0.86	0.08	0.87	0.13	0.74	0.29	0.76	0.29
PGAN-1	0.92	0.07	0.92	**0.09**	0.83	**0.25**	0.83	**0.26**
PGAN-2	0.92	0.06	**0.93**	**0.09**	**0.84**	**0.25**	**0.84**	0.27

the permittivity is high. It shows that the use of the perceptual adversarial loss in the proposed methods can still effectively improve the reconstruction quality for more challenging cases with high relative permittivities.

However, the results also indicate that the reconstruction quality of all methods drops quickly when the relative permittivity increases to 3.0. The reason is that the BP reconstruction in the first step cannot fully handle such high nonlinearity. This has also been observed when we test other profiles with permittivity as 3.0. More powerful coarse image reconstruction method needs to be developed to address the nonlinearity, which can ease the training difficulty of neural network in the second step.

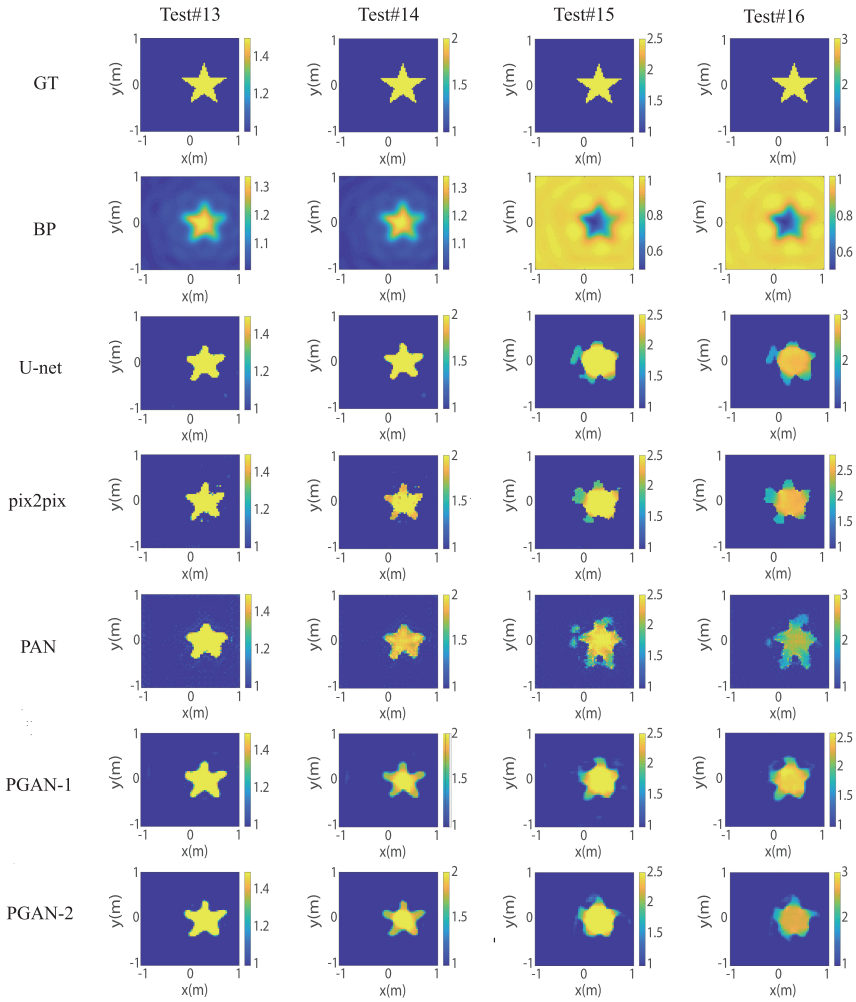

Fig. 8. Reconstruction results of different relative permittivity scatterers with 10% noise levels.

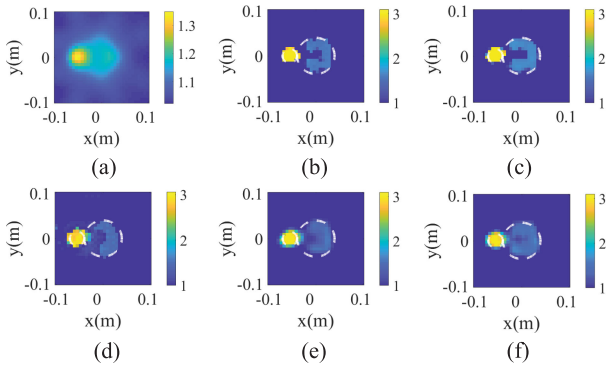

Fig. 9. Reconstruction results of "FoamDielExt" profiles at 3 GHz with (a) BP (b) U-net (c) pix2pix (d) PAN (e) PGAN-1 (f) PGAN-2.

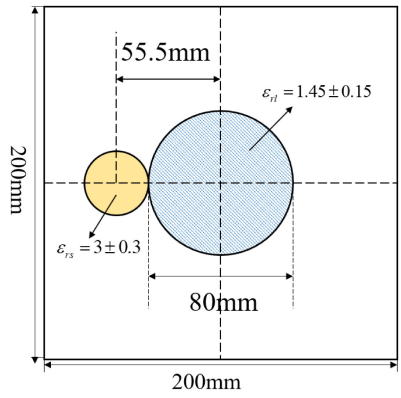

Fig. 10. The "FoamDielExt" profile from Fresnel experimental data.

E. Cross-Database Test: Experimental Data

Finally, we also validate the effectiveness of the proposed methods using experimental data measured by Institue Fresnel [40]. A "FoamDielExt" profile as shown in Fig. 10 is considered here with a TM case. The "FoamDielExt" profile consists of two cylinders, where the blue foam cylinder has a diameter of 80 mm with ε_r as 1.45 ± 0.15, and the yellow plastic cylinder has a diameter of 31 mm with ε_r as 3 ± 0.3. There are 8 linearly polarized transmitters and 241 co-polarized receivers, and the distance from the transmitter or receiver to the centre of the target is 1.67 m.

In this example, we use the same MNIST training profiles as the above synthetic examples, including the range of relative

TABLE VI
ERROR METRICS OF RECONSTRUCTION RESULTS IN FIG. 9 FOR EXPERIMENTAL DATA

Method	SSIM	RMSE
U-net	0.87	0.18
pix2pix	0.86	0.17
PAN	0.82	0.22
PGAN-1	0.86	0.18
PGAN-2	**0.89**	**0.15**

permittivity ε_r as those in the Section III-C, except that we change the frequency from 400 MHz to 3 GHz to be consistent with the experimental data. Accordingly, the size of DOI is also changed from 2.0 m $\times$ 2.0 m to 0.2 m $\times$ 0.2 m. In this example, all parameters of the perceptual loss are consistent with the above synthetic examples. But we need to retrain the model because of the different configurations and experimental settings in this example.

The reconstructed results of the "FoamDielExt" profile are shown in Fig. 9. Meanwhile, the SSIM and RMSE metrics of all methods are summarized in Table VI. It can be seen that the PGAN-2 achieves much better imaging quality, especially for the reconstruction of the large circle, in the experimental data. And the PGAN-1 has obtained similar results as the U-net and pix2pix methods. It also validates from this example that the proposed methods are effective and have good generalization capability when dealing with real inverse scattering data.

In summary, all the above results verify that the perceptual adversarial loss can effectively make the generator to explicitly learn the feature information of scatterers, and thereby enhancing the quality of reconstructions. The PGAN-2 method has achieved overall the best imaging quality for most cases. In contrast, the PGAN-1 may still outperform the PGAN-2 in few challenging cases due to the extra use of an adversarial loss. The simulation time of the PGAN methods in reconstructing a 64×64 image is around 0.86 seconds.

IV. CONCLUSION

In this paper, we have proposed a new deep learning-based method to solve ISPs with perceptual adversarial networks (PGAN). The BP method is employed to reconstruct a rough initial image, which is served as the input of the PGAN. The loss function of PGAN is composed by the perceptual adversarial loss, combined with the pixel-wise loss, and also possibly the adversarial loss, to enforce a multi-level match of pixels and features between the reconstructed and reference images. The comparisons of the proposed method on both synthetic and experimental data validate that the proposed PGAN can effectively improve the reconstruction performance in terms of both the accuracy and the generalization capability. Although we only use one hidden layer to define the perceptual adversarial loss in this paper, more hidden layers can also be employed for imaging complex targets in medical imaging and non-destructive testing.

REFERENCES

[1] M. Uecker, T. Hohage, K. T. Block, and J. Frahm, "Image reconstruction by regularized nonlinear inversion-joint estimation of coil sensitivities and image content," *Magn. Reson. Med.*, vol. 60, no. 3, pp. 674–682, Sep. 2008.

[2] T. Deisboeck and J. Y. Kresh, *Complex Systems Science in Biomedicine*. New York, NY, USA: Springer Science & Business Media, 2007.

[3] L.-P. Song, C. Yu, and Q. H. Liu, "Through-wall imaging (TWI) by radar: 2-D tomographic results and analyses," *IEEE Trans. Geosci. Remote Sens.*, vol. 43, no. 12, pp. 2793–2798, Dec. 2005.

[4] T. M. Habashy, R. W. Groom, and B. R. Spies, "Beyond the Born and Rytov approximations: A nonlinear approach to electromagnetic scattering," *J. Geophysical Res.: Solid Earth*, vol. 98, no. B2, pp. 1759–1775, 1993.

[5] K. Belkebir, P. C. Chaumet, and A. Sentenac, "Superresolution in total internal reflection tomography," *J. Opt. Soc. Amer. A*, vol. 22, no. 9, pp. 1889–1897, 2005.

[6] X. Chen, *Computational Methods for Electromagnetic Inverse Scattering*. New York, NY, USA: Wiley-IEEE Press, 2018.

[7] W. C. Chew and Y.-M. Wang, "Reconstruction of two-dimensional permittivity distribution using the distorted Born iterative method," *IEEE Trans. Med. Imag.*, vol. 9, no. 2, pp. 218–225, Jun. 1990.

[8] P. M. Van DenBerg and R. E. Kleinman, "A contrast source inversion method," *Inverse Problems*, vol. 13, no. 6, 1997, Art no. 1607.

[9] X. Chen, "Subspace-based optimization method for solving inverse-scattering problems," *IEEE Trans. Geosci. Remote Sens.*, vol. 48, no. 1, pp. 42–49, Jan. 2010.

[10] S. Caorsi and P. Gamba, "Electromagnetic detection of dielectric cylinders by a neural network approach," *IEEE Trans. Geosci. Remote Sens.*, vol. 37, no. 2, pp. 820–827, Mar. 1999.

[11] I. T. Rekanos, "Neural-network-based inverse-scattering technique for online microwave medical imaging," *IEEE Trans. Magn.*, vol. 38, no. 2, pp. 1061–1064, Mar. 2002.

[12] U. Aşık, T. Günel, and I. Erer, "A wavelet-based radial-basis function neural network approach to the inverse scattering of conducting cylinders," *Microw. Opt. Technol. Lett.*, vol. 41, no. 6, pp. 506–511, 2004.

[13] A. Massa, G. Oliveri, M. Salucci, N. Anselmi, and P. Rocca, "Learning-by-examples techniques as applied to electromagnetics," *J. Electromagn. Waves Appl.*, vol. 32, no. 4, pp. 516–541, 2018.

[14] A. Krizhevsky, I. Sutskever, and G. E. Hinton, "Imagenet classification with deep convolutional neural networks," in *Proc. Adv. Neural Inf. Process. Syst.*, 2012, pp. 1097–1105.

[15] K. Simonyan and A. Zisserman, "Very deep convolutional networks for large-scale image recognition," in *Proc. Int. Conf. Learn. Representations*, 2014.

[16] J. Du and Y. Xu, "Hierarchical deep neural network for multivariate regression," *Pattern Recognit.*, vol. 63, pp. 149–157, 2017.

[17] Y. Sanghvi, Y. Kalepu, and U. K. Khankhoje, "Embedding deep learning in inverse scattering problems," *IEEE Trans. Comput. Imag.*, vol. 6, pp. 46–56, May 2019.

[18] R. Guo *et al.*, "Pixel-and model-based microwave inversion with supervised descent method for dielectric targets," *IEEE Trans. Antennas Propag.*, vol. 68, no. 12, pp. 8114–8126, Dec. 2020.

[19] T. Song, L. Kuang, L. Han, Y. Wang, and Q. H. Liu, "Inversion of rough surface parameters from SAR images using simulation-trained convolutional neural networks," *IEEE Geosci. Remote Sens. Lett.*, vol. 15, no. 7, pp. 1130–1134, Jul. 2018.

[20] X. Chen, Z. Wei, M. Li, and P. Rocca, "A review of deep learning approaches for inverse scattering problems (*invited review*)," *Prog. Electromagnetics Res.*, vol. 167, pp. 67–81, 2020.

[21] L. Zhang, K. Xu, R. Song, X. Z. Ye, G. Wang, and X. Chen, "Learning-based quantitative microwave imaging with a hybrid input scheme," *IEEE Sensors J.*, vol. 20, no. 24, pp. 15007–15013, Dec. 2020.

[22] Z. Wei and X. Chen, "Physics-inspired convolutional neural network for solving full-wave inverse scattering problems," *IEEE Trans. Antennas Propag.*, vol. 67, no. 9, pp. 6138–6148, Sep. 2019.

[23] H. M. Yao, E. Wei, and L. Jiang, "Two-step enhanced deep learning approach for electromagnetic inverse scattering problems," *IEEE Antennas Wireless Propag. Lett.*, vol. 18, no. 11, pp. 2254–2258, Nov. 2019.

[24] H. M. Yao, L. Jiang, and E. Wei, "Enhanced deep learning approach based on the deep convolutional encoder-decoder architecture for electromagnetic inverse scattering problems," *IEEE Antennas Wireless Propag. Lett.*, vol. 19, no. 7, pp. 1211–1215, Jul. 2020.

[25] Y. Huang, R. Song, K. Xu, X. Ye, C. Li, and X. Chen, "Deep learning based inverse scattering with structural similarity loss functions," *IEEE Sensors J.*, vol. 21, no. 4, pp. 4900–4907, Feb. 2021.

[26] X. Ye, Y. Bai, R. Song, K. Xu, and J. An, "An inhomogeneous background imaging method based on generative adversarial network," *IEEE Trans. Microw. Theory Techn.*, vol. 68, no. 11, pp. 4684–4693, Nov. 2020.

[27] G. Ian *et al.*, "Generative adversarial nets," *Adv. Neural Inf. Process. Syst.*, vol. 2, pp. 2672–2680, 2014.

[28] C. Ledig *et al.* "Photo-realistic single image super-resolution using a generative adversarial network," in *Proc. IEEE Conf. Comput. Vis. Pattern Recognit.*, 2017, pp. 4681–4690.

[29] J. Johnson, A. Alahi, and L. Fei-Fei, "Perceptual losses for real-time style transfer and super-resolution," in *Proc. Eur. Conf. Comput. Vis.*, 2016, pp. 694–711.

[30] Q. Yang *et al.*, "Low-dose CT image denoising using a generative adversarial network with wasserstein distance and perceptual loss," *IEEE Trans. Med. Imag.*, vol. 37, no. 6, pp. 1348–1357, Jun. 2018.

[31] C. Wang, C. Xu, C. Wang, and D. Tao, "Perceptual adversarial networks for image-to-image transformation," *IEEE Trans. Image Process.*, vol. 27, no. 8, pp. 4066–4079, Aug. 2018.

[32] Z. Wei and X. Chen, "Deep-learning schemes for full-wave nonlinear inverse scattering problems," *IEEE Trans. Geosci. Remote Sens.*, vol. 57, no. 4, pp. 1849–1860, Apr. 2019.

[33] O. Ronneberger, P. Fischer, and T. Brox, "U-net: Convolutional networks for biomedical image segmentation," in *Proc. Int. Conf. Med. Image Comput. Comput.-Assist. Intervention*, 2015, pp. 234–241.

[34] P. Isola, J.-Y. Zhu, T. Zhou, and A. A. Efros, "Image-to-image translation with conditional adversarial networks," in *Proc. IEEE Conf. Comput. Vis. Pattern Recognit.*, 2017, pp. 1125–1134.

[35] A. Devaney, "Geophysical diffraction tomography," *IEEE Trans. Geosci. Remote Sens.*, vol. GE-22, no. 1, pp. 3–13, Jan. 1984.

[36] L. Li, L. G. Wang, J. Ding, P. Liu, M. Xia, and T. J. Cui, "A probabilistic model for the nonlinear electromagnetic inverse scattering: TM case," *IEEE Trans. Antennas Propag.*, vol. 65, no. 11, pp. 5984–5991, Nov. 2017.

[37] A. Massa, D. Marcantonio, X. Chen, M. Li, and M. Salucci, "DNNs as applied to electromagnetics, antennas, and propagation—A review," *IEEE Antennas Wireless Propag. Lett.*, vol. 18, no. 11, pp. 2225–2229, Nov. 2019.

[38] J. Cong and B. Xiao, "Minimizing computation in convolutional neural networks," in *Proc. Int. Conf. Artif. Neural Netw.*, 2014, pp. 281–290.

[39] Y. LeCun, L. Bottou, Y. Bengio, and P. Haffner, "Gradient-based learning applied to document recognition," *Proc. IEEE*, vol. 86, no. 11, pp. 2278–2324, Nov. 1998.

[40] J.-M. Geffrin, P. Sabouroux, and C. Eyraud, "Free space experimental scattering database continuation: Experimental set-up and measurement precision," *Inverse Problems*, vol. 21, no. 6, 2005, Art no. S 117.

[41] K. Belkebir and A. Tijhuis, "Using multiple frequency information in the iterative solution of a two-dimensional nonlinear inverse problem," in *Proc. Prog. Electromagnetics Res. Symp., PIERS 1996, 8 Jul. 1996, Innsbruck, Germany*. Universität Innsbruck, 1996, p. 353.